



RESEARCH ARTICLE

Response of drylands' water-cycle to the global warming

Min Luo¹ | Yuzhi Liu^{1,2}  | Tianbin Shao¹ 

¹Key Laboratory for Semi-Arid Climate Change of the Ministry of Education, College of Atmospheric Sciences, Lanzhou University, Lanzhou, China

²Collaborative Innovation Center for Western Ecological Safety, Lanzhou University, Lanzhou, China

Correspondence

Yuzhi Liu, Key Laboratory for Semi-Arid Climate Change of the Ministry of Education, College of Atmospheric Sciences, Lanzhou University, Lanzhou, 730000, China.
Email: liuyzh@lzu.edu.cn

Funding information

the National Natural Science Foundation of China, Grant/Award Numbers: 41991231, 91744311, 41521004, 91937302; Strategic Priority Research Program of Chinese Academy of Sciences, Grant/Award Number: XDA2006010301; the Fundamental Research Funds for the Central Universities, Grant/Award Number: lzujbky-2020-kb02

Abstract

Drylands occupy about 41% of land surface and feed 38% of the world's population, where understanding drylands' water-cycle is in urgent need. In this study, response of water-cycle over the drylands to global warming from 1980 to 2015 and its mechanisms have been investigated in detail. The results show that, with the global surface air temperature (SAT) increasing at a rate of 0.03 K·year⁻¹ over the drylands, an increased evaporation is found; however, the net water vapour transport over the global drylands appears an overall decreased rate of -0.24 mm·year⁻¹. Due to global warming and atmospheric circulation anomalies, the evaporation increases by 1.1 mm·year⁻¹, while the precipitation and runoff decrease by -2.32 and -0.8 mm·year⁻¹, respectively. In addition, the precipitation conversion rate (PCR) tends to decrease during this period, while the precipitation recycling rate (PRR) shows slightly increasing trend, implying a more dependence of the precipitation on the local evaporation over the drylands. Overall, except the drylands of Africa, it indicates a weakened water-cycle over the global drylands from 1980 to 2015. Though some findings have been revealed, there still remains some uncertainties due to the observation limitation on the water-cycle components. Therefore, a comprehensive study including multi-sourced data and model simulation is expected in the future.

KEYWORDS

drylands, global warming, precipitation conversion rate, precipitation recycling rate, water-cycle

1 | INTRODUCTION

Water-cycle is a continuous circulation of water through ocean, atmosphere, land surface and subsurface. Among the processes involved in the water-cycle, the most important are precipitation, evaporation, runoff and condensation (Yin and Roderick, 2020). Generally, the water is transferred from the Earth's surface to the atmosphere by evaporation, being the primary form of atmospheric moisture. Then, by condensation, water vapour in the atmosphere is released to precipitation. The precipitation falling on the land surface is distributed in four main ways: some is returned to the atmosphere by evaporation,

some may be intercepted by vegetation and then evaporates from the surface of leaves, some percolates into the soil by infiltration, and the remainder flows directly as runoff into the sea (Gimeno *et al.*, 2012). Under the background of global warming, the frequency of extreme climate events and anomaly of water-cycle increase significantly. Therefore, water-cycle is an important issue which is tightly linked to the human living environment.

Water-cycle could be affected by natural factors including ocean salinity pattern (Skirris *et al.*, 2020), solar insolation change (Fu *et al.*, 2009; Wang *et al.*, 2012, 2013; Qi *et al.*, 2013), volcanic eruptions (Alfaro-Sánchez *et al.*, 2018), and the internal variation of climate change

(Song *et al.*, 2014). Meanwhile, it can be also altered by human activities including pollutants (Hua *et al.*, 2018; Liu *et al.*, 2019a, 2019b, 2019c, 2019d; Luo *et al.*, 2020a), irrigation (Grafton *et al.*, 2018), and land use change (Abbott *et al.*, 2019; Li *et al.*, 2019; Allan *et al.*, 2020). With the global warming, the anomalous water-cycle is increasingly dominated by the human activities (Allan *et al.*, 2020). It is urgent to understand the water-cycle response to the global climate change.

Generally, the drylands relate significantly to the global climate change (Huang *et al.*, 2008). Due to low fertility of soil and deficiency of water resources, the global drylands are extremely facing the risk of degradation and expansion (Scheffer *et al.*, 2001; Huang *et al.*, 2017; Liu *et al.*, 2018), which could in turn affect the water-cycle. Recently, much effort has been made to reveal the changes in drylands' water-cycle. Many researchers revealed that, due to lack of water resources, the atmospheric water vapour over the drylands is primarily originated from external transport (Xu *et al.*, 2016). For the African arid region, the water vapour transported from Mediterranean Sea plays a critical role in the local rainfall (Fontaine *et al.*, 2003). Besides, the water vapour over East Asian arid region originates mainly from the Northwest Pacific Ocean and the Bengal Bay (Han *et al.*, 2016; Liu *et al.*, 2018). Due to the increases in evaporation and precipitation, the global water-cycle is found to be intensified over monsoon regions (Dwyer *et al.*, 2014; Zhang *et al.*, 2019). Furthermore, the increased precipitable water usually implies the increased residence time of water vapour in the atmosphere under the global warming background, which leads to a weakening water-cycle on the global scales (Bosilovich *et al.*, 2005). Thus, the water-cycle presents different features over different regions.

Usually, to reveal the contribution of local evaporation to precipitation, the precipitation recycling rate (PRR) is introduced. Previous studies reported that the PRR over drylands indicates more advantages than that over humid regions (Li *et al.*, 2018). It was found that the PRR tends to decrease over the arid area of western Tibetan Plateau, North America and North Africa during period 1979–2012, while it tends to increase over Asia (Guo and Wang, 2014; Li *et al.*, 2018). Additionally, the PRR increased significantly from 1980s to the early 21st century over the arid area of the northwestern China (Yao *et al.*, 2020). Though some findings have been obtained, there remain huge uncertainties of quantifying PRR over the global drylands due to the limitation of data sets. In addition, under an enhance warming climate (Guan *et al.*, 2015) and expanded global drylands (Huang *et al.*, 2016a, 2016b), it may induce the rising of CO₂ and decreasing of O₂, which has a significant influence on the eco-system and global water-cycle (Huang *et al.*, 2018).

Thus, understanding the response of water-cycle is becoming a critical issue to perform the sustainable development over the drylands.

In this study, a systematic analysis of water-cycle over global drylands is performed. The descriptions of data sets are presented in Section 2. The methods are shown in Section 3. Furthermore, the trends of water-cycle components, the changed precipitation conversion rate (PCR), PRR, a comprehensive analysis on the features and intensity of water-cycle are shown in Section 4. Discussions and the conclusions are presented in Section 5.

2 | DATA SETS

2.1 | ERA5 reanalysis data

ERA5 reanalysis product is the fifth generation European Centre for Medium-Range Weather Forecasts (ECMWF) reanalysis for the global climate and weather. Previous research showed that the correlation of ERA5 reanalysis with the Global Precipitation Climatology Project (GPCP) data has been more significantly increased than ERA-interim data set (Hersbach *et al.*, 2020). It shows a more apparent improvement for temperature, wind field, humidity in the troposphere than ERA-interim. Basing on ERA5 data, the monthly precipitation (P), evaporation (E), runoff, soil water (SW), surface air temperature (SAT), surface pressure and the horizontal wind (u and v components), vertical velocity, specific humidity (q) with a spatial resolution of $0.25^\circ \times 0.25^\circ$ from surface to 200 hPa during the period of 1980–2015 are used. During analysis, to match the resolution of CRU data, we have interpolated the ERA5 data from resolution of $0.25^\circ \times 0.25^\circ$ to $0.5^\circ \times 0.5^\circ$. The accumulated period of monthly mean precipitation, evaporation and runoff is 1 day.

Meanwhile, the evaporation data of ERA5 just include a simplified representation of transpiration from vegetation through considering the surface energy budget and physical constraints of soil moisture (Hersbach *et al.*, 2020). In ERA5, the revised hydrology scheme of land surface (HTESSEL) is used (Balsamo *et al.*, 2015). Besides, the other significant changes are related to the introduction of the soil texture map (Balsamo *et al.*, 2009) and the representation of evaporation over bare soil (Albergel *et al.*, 2012). The data sets of ERA5 can account for monthly vegetation maps specified from MODIS-based satellite data set (Boussetta *et al.*, 2013). It may not fully account for vegetation responses under the rising CO₂ and global warming. Even, there is a risk of over-estimating the evaporation. Because of the scarcity of meteorological observations over the global drylands, the ERA5 data still have the irreplaceable advantages in

studying the water-cycle over the global drylands (Hersbach *et al.*, 2020; Pelosi *et al.*, 2020).

2.2 | Climate research unit data

The data of climate research unit (CRU) are obtained from the meteorological site observations in the world. Although the CRU data contains errors caused by interpolation, it can still be used as a reference with certain reliability. The availability of CRUv4 temperature has been estimated by adjusting the variance of each grid box (Brohan *et al.*, 2006). In this study, the monthly precipitation and potential evapotranspiration (*PET*) data from CRUv4 with a spatial resolution of $0.5^\circ \times 0.5^\circ$ are used to calculate the aridity index.

3 | ANALYTICAL METHODOLOGY

3.1 | Water vapour transport budget

The vertically integrated water vapour flux (*Q*) is calculated from the land surface to 200 hPa as follows:

$$Q = \frac{1}{g} \int_{P_s}^{P_t} q \vec{V} dp \tag{1}$$

Where *q* denotes the specific humidity ($\text{kg}\cdot\text{kg}^{-1}$), \vec{V} refers to the horizontal wind (like *u* and *v* component, $\text{m}\cdot\text{s}^{-1}$), and *g* indicates the value of gravity acceleration which approximates to $9.8 \text{ m}\cdot\text{s}^{-2}$. *P_t* and *P_s* denote the pressure at the top of atmosphere and surface, respectively. In this study, *P_t* is taken as 200 hPa.

Then, the water vapour budget (*B*) is calculated according to Zhou *et al.* (2019):

$$B = \oint Q dl \tag{2}$$

Where *l* denotes four borders of each region, including east, south, west and north borders presented in Figure 1.

3.2 | PCR

The atmospheric precipitable water (*PW*) is calculated from land surface to 200 hPa by Equation (3). The calculation of *PCR* is presented as Equation (4):

$$PW = -\frac{1}{g} \int_{P_s}^{P_t} q dp \tag{3}$$

$$PCR = \frac{P}{PW} \tag{4}$$

Where the *g*, *P_t* and *P_s* in Equation (3) are the same with the parameters in Equation (1). *PW* is calculated by the monthly mean specific humidity. Besides, the *PCR* in Equation (4) is calculated by the mean precipitable water and precipitation during 1980–2015.

3.3 | PRR

The *PRR* describes the contribution of local evaporation to precipitation. To calculate the *PRR*, two hypotheses are proposed: water vapour in the atmosphere is well

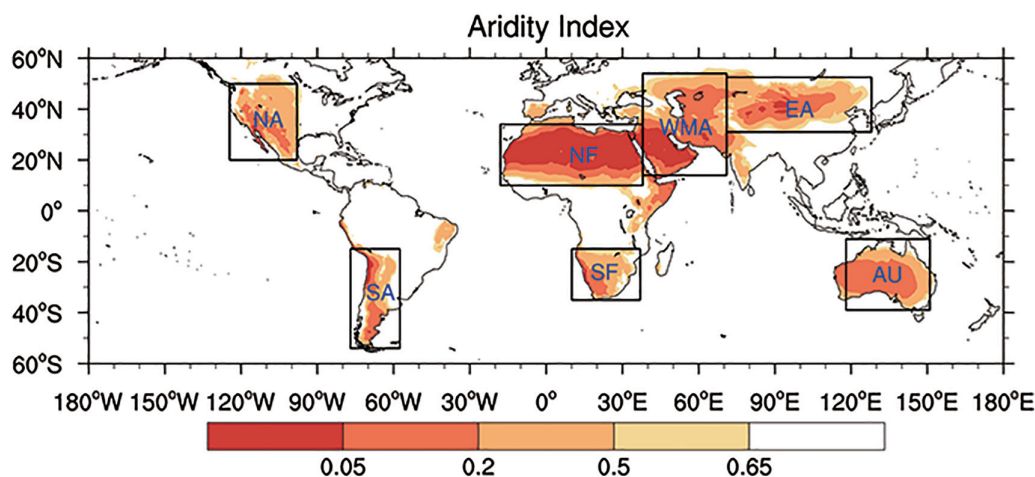


FIGURE 1 Distribution of the global drylands defined by the aridity index (AI). The regions enclosed by rectangles denote the drylands over East Asia (EA), West and Central Asia (WMA), North Africa (NF), South Africa (SF), North America (NA), South America (SM), Australia (AU) [Colour figure can be viewed at wileyonlinelibrary.com]

mixed and the exported water vapour at each grid is neglected (Guo and Wang, 2014; Su *et al.*, 2014; Li *et al.*, 2018). Generally, the evaporation can be calculated by the law of conservation of mass neglecting the changes in atmospheric column water vapour content (Brubaker *et al.*, 1993). A revised calculation of evaporation considering the changes in atmospheric column water vapour content can be presented as follows:

$$E \approx P + \nabla \cdot \vec{Q} \quad (5)$$

Where E , P and $\nabla \cdot \vec{Q}$ denote the revised evaporation, precipitation and water vapour flux divergence, respectively.

$$Q_a = \frac{F_{in} + (F_{in} - P_a A)}{2} = F_{in} - \frac{P_a A}{2} \quad (6)$$

Where F_{in} denotes the imported water vapour over drylands, P_a is the contribution of external imported water vapour to the local precipitation. A denotes the area of study region. The imported water vapour (Q_a) can be calculated by the arithmetic mean of import (F_{in}) and export ($F_{in} - P_a A$) water vapour.

Similarly, the flux of local evaporation (Q_m) can be calculated as follows:

$$Q_m = \frac{0 + (E - P_m)A}{2} = \frac{(E - P_m)A}{2} \quad (7)$$

Where E denotes the revised evaporation described by Equation (5), P_m denotes the contribution of local evaporation to precipitation.

$$PRR = \frac{P_m}{P} = \frac{Q_m}{Q_m + Q_a} = \frac{EA}{EA + 2 \times F_{in}} \quad (8)$$

It is supposed that the atmospheric water vapour originated from different sources is well mixed. The PRR, defined as the ratio of P_m/P (equals to Q_a/Q_m), is performed at the grid scale. Combined the formulas (6) and (7), the PRR can be expressed as Equation (8).

3.4 | The annual range

The annual range (AR) can describe the intensity of water-cycle well. In addition, it is defined as the difference between the monthly maximum (V_{max}) and minimum (V_{min}) values within 1 year (Chou and Lan, 2012; Zhang *et al.*, 2019). AR is expressed as follows:

$$AR = V_{max} - V_{min} \quad (9)$$

4 | ANALYSIS AND RESULTS

Generally, the dryland implies the region where the PET greatly exceeds the total precipitation (Hulme, 1996). The degree of drought can be described by the ratio of P/PET which is defined as the aridity index (AI). According to the values of AI , the hyper arid, arid, semi-arid and sub-humid regions are classified when $AI < 0.05$, $0.05 \leq AI < 0.2$, $0.2 \leq AI < 0.5$ and $0.5 \leq AI < 0.65$, respectively (Huang *et al.*, 2017). Here, we focus mainly on the drylands including arid and semi-arid regions, where $AI < 0.65$, enclosed by the rectangles in Figure 1.

In the analysis, the global drylands are divided into the drylands over East Asia (EA, 71°E–128°E, 31°N–52°N), West and Central Asia (WMA, 38°E–71°E, 14°N–52°N), North Africa (NF, 18°W–38°E, 10°N–34°N), North America (NA, 98°W–124°W, 20°N–50°N), South America (SA, 57°W–77°W, 15°S–54°S), South Africa (SA, 10°E–37°E, 15°S–35°S), and Australia (AU, 118°E–151°E, 11°S–39°S). It is found that the drylands are mainly located at the mid-latitudes (around 30°N or 30°S) because of the descending branch of Hadley circulation and the Subtropical High (Ping *et al.*, 2001; Shin *et al.*, 2012). Besides, the ‘Foehn Effect’ caused by the high mountains on the leeward side in NA and SA is conducive to local drought also.

4.1 | Changes in SAT over the drylands

Figure 2 describes the changes in SAT over the global drylands from 1980 to 2015. The result shows that the warming trend of global drylands is about 0.03 K·year⁻¹ (Figure 2b), with the maximum trend reaching 0.06 K·year⁻¹ in the drylands of NF and Asia. East Asian drylands have a warming trend of 0.04 K·year⁻¹ (Figure 2e), which is in consistent with the result reported by Luo *et al.* (2020b). Meanwhile, the warming over the drylands of NA, SA, NF, SF and AU is about 0.03, 0.02, 0.04, 0.02 and 0.02 K·year⁻¹, respectively. It implies a significant climate warming during the period 1980–2015 over the global drylands, which is agreement with the findings of Huang *et al.* (2017).

4.2 | Responses of evaporation, precipitation and cloud over drylands

With the global warming, the evaporation experienced an increased trend, inducing the atmospheric water vapour increases by 7%/°C in the low atmosphere (Allan

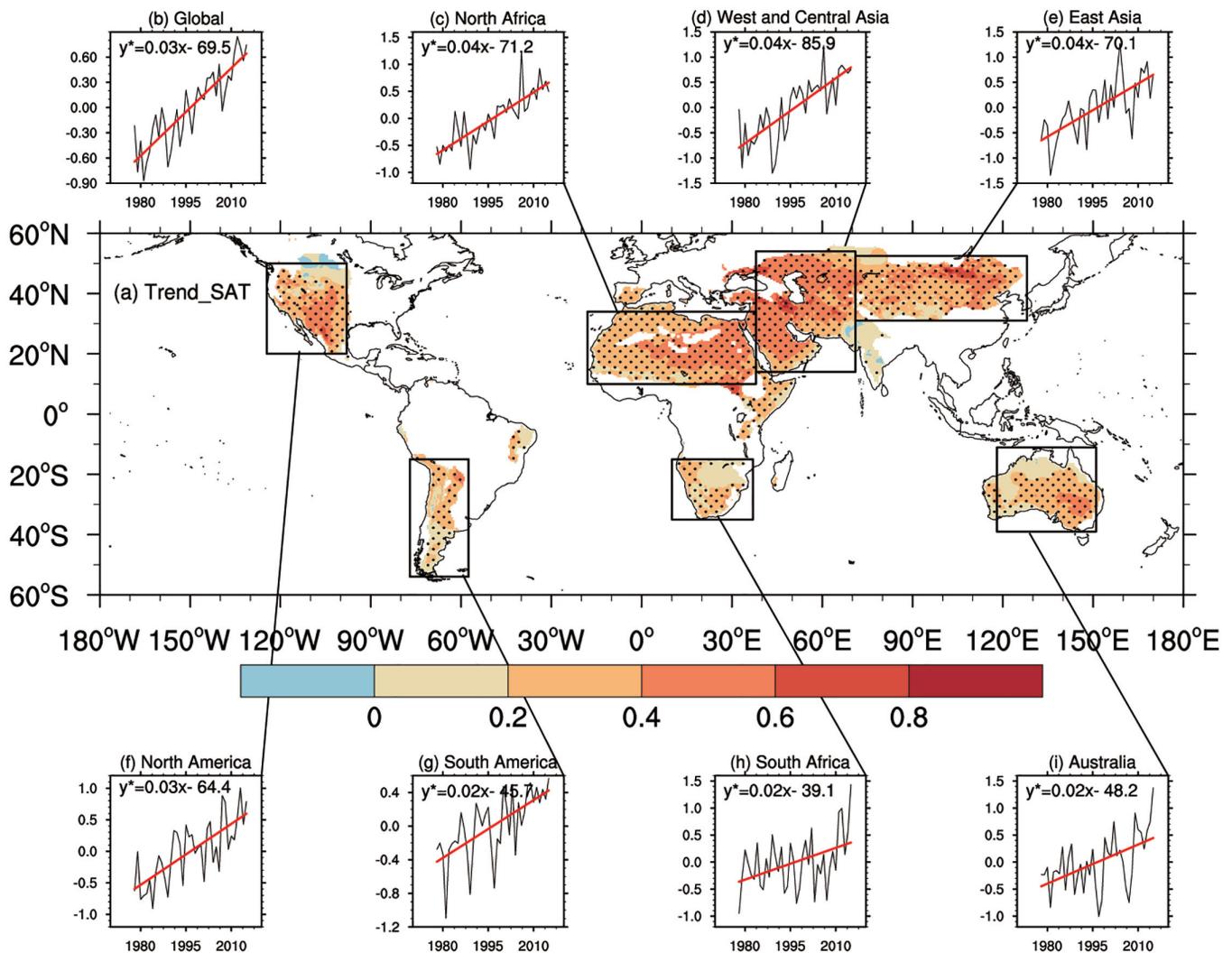


FIGURE 2 Trends of SAT from 1980 to 2015 (unit: $\text{K}\cdot\text{year}^{-1}$). The dots denote the trends are significant above the 90% confidence level. The curve panels (b–i) show the time series of SAT over different drylands, in which the straight lines refer to the linear fitting trend. Lable * in the linear equation indicates the trend is significant above the 90% confidence level. The regions enclosed by rectangles denote the typical drylands in the globe, as described at the bottom of Figure 1 [Colour figure can be viewed at wileyonlinelibrary.com]

et al., 2014). In return, the increased atmospheric water vapour, as an important greenhouse gas, will exert a stronger warming effect (Zhang *et al.*, 2018). In the following, the responses of evaporation, precipitation and cloud to the climate warming over the global drylands are investigated. Figure 3 indicates the tendencies of evaporation, precipitation and $P-E$ (precipitation minus evaporation) from 1980 to 2015. The result shows that the evaporation over different drylands, except the arid regions of Northwest China, parts of NF and SF, tends to increase during period 1980–2015. The maximum trend is found over the drylands of NA, SA and AU with the value larger than $0.6 \text{ mm}\cdot\text{year}^{-1}$ (Figure 3a). The evaporation over North China and WMA tends to increase by $0.15\text{--}0.3 \text{ mm}\cdot\text{year}^{-1}$. Furthermore, Figure 3b shows that the precipitation over the drylands of Northeast China,

WMA, AU, NA and SA tends to decrease with the minimum of $-0.6 \text{ mm}\cdot\text{year}^{-1}$. On the contrary, the precipitation over the drylands of Northwest China, NF and SF shows increasing with the maximum trend of $0.60 \text{ mm}\cdot\text{year}^{-1}$. Moreover, the pattern of $P-E$ is similar with that of precipitation (Figure 3c). The increased (decreased) $P-E$ over the drylands of NF and SF (EA, WMA, NA, SA and AU) means more (less) terrestrial water storage.

Global warming can affect not only the evaporation and precipitation but also the formation of cloud by disturbing the atmospheric circulation and water vapour transport (IPCC, 2013). Figure 4 shows the distribution of cloud cover and cloud water trends. It indicates that the cloud cover, cloud liquid water (CLW) and cloud ice water (CIW) present increased trends over the drylands

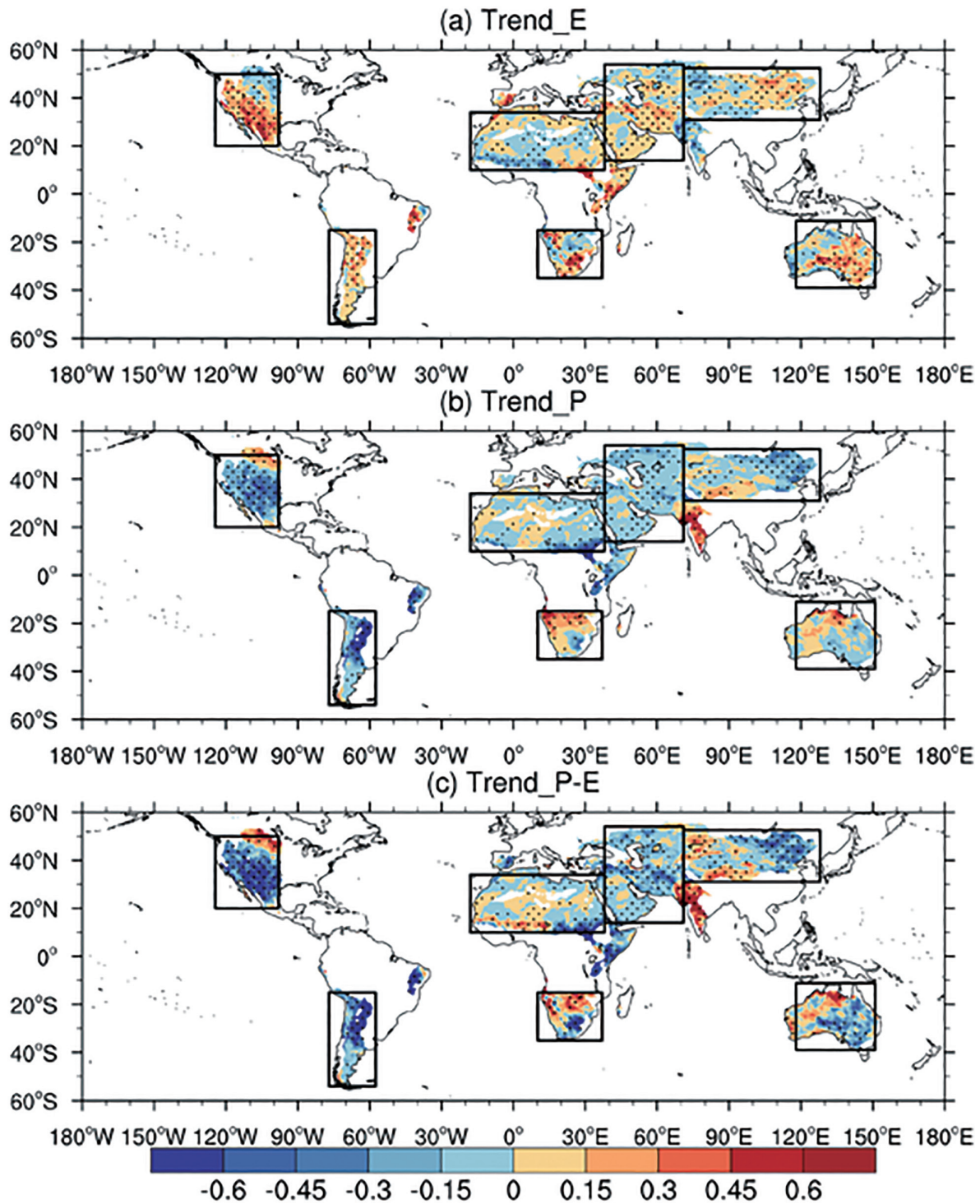


FIGURE 3 Trends of (a) evaporation, (b) precipitation and (c) the P-E (unit: mm year^{-1}). The dots denote the trends are significant above the 90% confidence level. The regions enclosed by rectangles denote the typical drylands in the globe, as described at the bottom of Figure 1 [Colour figure can be viewed at wileyonlinelibrary.com]

of Northwest China and Africa, but decreasing trends over the drylands of Northeast China, WME, NA and SA. The results are consistent with the recent studies (Xiang *et al.*, 2014; Lei *et al.*, 2015). The changes in cloud cover and cloud water are closely related to the

adjustment of atmospheric circulation. The enhanced upward motions could cause the increase in cloud cover and cloud water, while the weakened upward motions could result in a decrease in cloud cover and cloud water.

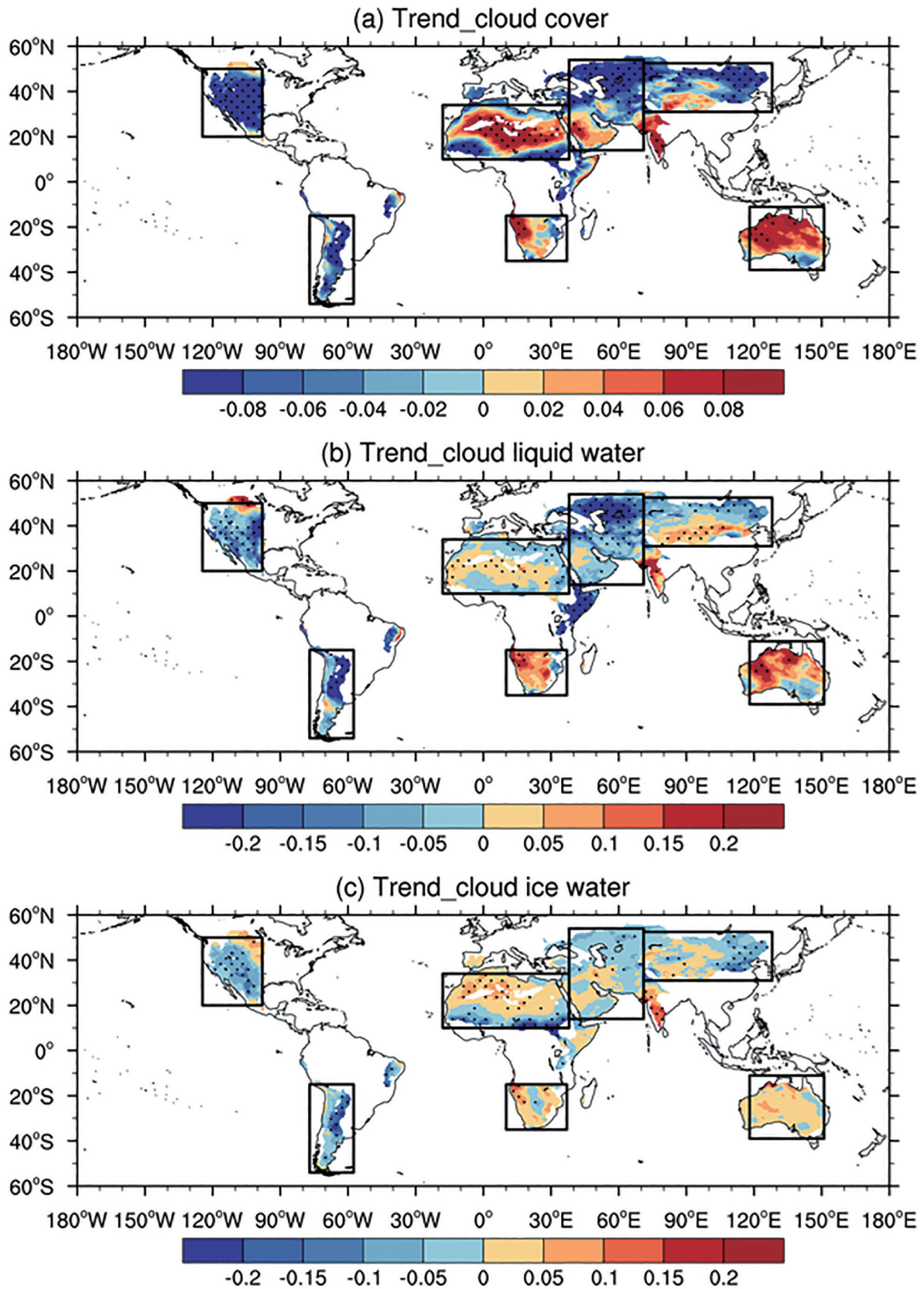


FIGURE 4 Trends of (a) cloud cover (unit: %·year⁻¹), (b) cloud liquid water path, and (c) cloud ice water path (unit: g·m⁻²·year⁻¹). The dots denote the trends are significant above the 90% confidence level. The regions enclosed by rectangles denote the typical drylands in the globe, as described at the bottom of Figure 1 [Colour figure can be viewed at wileyonlinelibrary.com]

4.3 | Responses of PCR and PRR

Figure 5a shows the distribution of water vapour flux and trend during period 1980–2015. The result shows that the water vapour transport over the equator region is dominated by the easterlies, while the transport over the mid-latitude region is dominated by the westerlies. The easterlies over the equator region and westerlies over the mid-latitude region show significantly strengthened trends from 1980 to 2015, which exerts profound effect on the water vapour budget. It is found that the exported water vapour along the east border of EA drylands tends to increase evidently, while the water vapour imported from southwest border shows significantly decreasing trend. Thus, more exported water vapour from the drylands of EA results in a negative water vapour budget.

For the drylands of WME, NA and SA, the increases in exported water vapour contribute negative budget also. For the drylands of NF, more imported water vapour from north border causes a positive budget there. Figure 5b indicates the net water vapour budget over each region. The result presents that the mean water vapour budget is about -1.25 mm over the global drylands during the past 36 years from 1980 to 2015. The maximum positive water vapour budget is found over the drylands of NF with the value of 1.61 mm. However, the maximum negative budget is found in the drylands of NA with the value of -3.54 mm. For the drylands of EA and AU, the negative water vapour budgets are -2.89 and -2.3 mm, respectively.

The values and changes in PCR and PRR can reflect the internal water-cycle of drylands. Figure 6 gives the

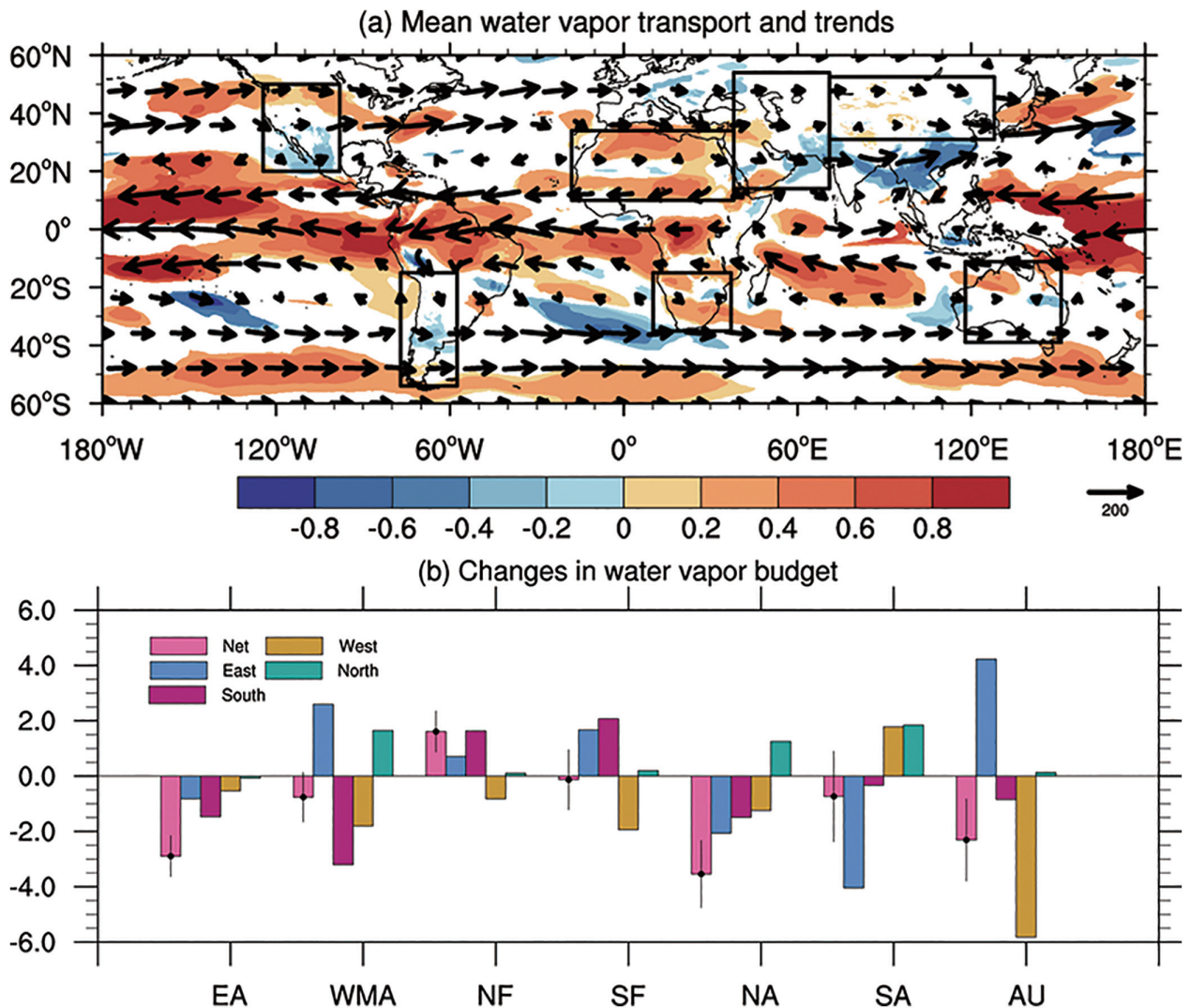


FIGURE 5 (a) The mean atmospheric water vapour flux from surface to 200 hPa (vector, unit: $\text{kg}\cdot\text{m}^{-1}\cdot\text{s}^{-1}$) and trends distribution (shaded), and the (b) the net water vapour budget (mm) over the global drylands from 1980 to 2015. The short straight lines in (b) denote the SE. The regions enclosed by rectangles in (a) denote the typical drylands in the globe, as described at the bottom of Figure 1 [Colour figure can be viewed at wileyonlinelibrary.com]

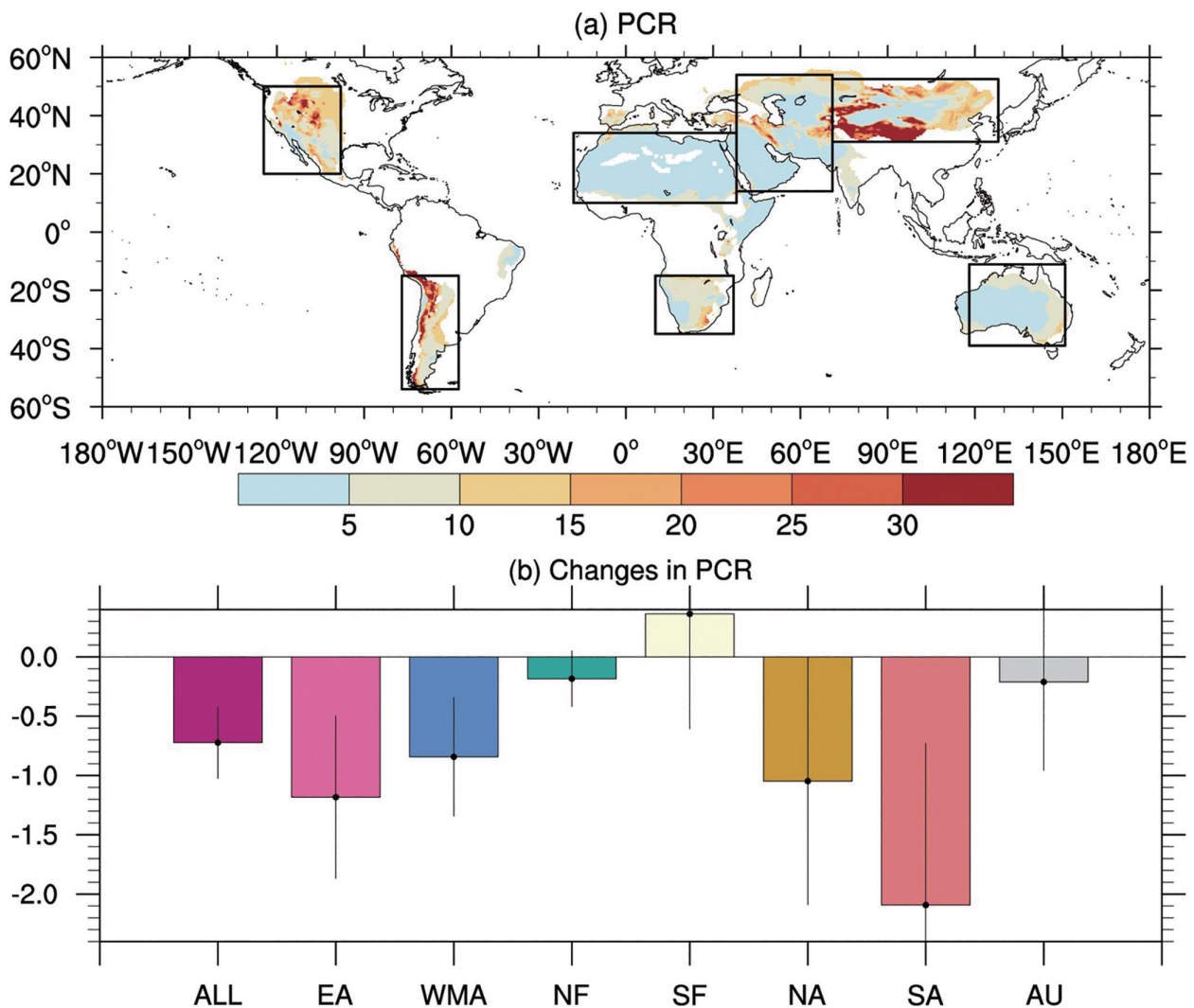


FIGURE 6 (a) Distribution (a) of PCR (unit: %) and (b) the changes in the PCR over global drylands during period 1980–2015. The short straight lines in (b) denote the *SE*. The regions enclosed by rectangles in (a) denote the typical drylands in the globe, as described at the bottom of Figure 1 [Colour figure can be viewed at wileyonlinelibrary.com]

changes in PCR over the global drylands from 1980 to 2015. The result shows that the values of PCR over the drylands of WMA, NF, SF and AU are less than 10%, while the PCRs are greater than those over the drylands of EA, NA and SA (Figure 6a). From 1980 to 2015, the global PCR indicates an overall decreasing (-0.7%), and the maximum decrease in PCR is found over the drylands of SA with the value of -2.0% (Figure 6b). The decrease in PCR indicates a longer time of the water vapour remaining in the atmosphere, which could weaken the local water-cycle.

In addition, the PRR can describe the contribution of local evaporation to the precipitation (Burde and Zangvil, 2001). Figure 7 shows the distributions and changes of PRR over different regions during the past 36 years (1980–2015). The result shows that the average

PRR over the drylands of NF and AU can reach 16%, which is obviously greater than that over the other drylands (Figure 7a). It implies a more obvious dependence of the precipitation on the local evaporation over the NF and AU drylands. On the contrary, the precipitation over the drylands of EA, NA and SA depends more on the external water vapour transport. Overall, the PRR over the global drylands increases by about 5% (Figure 7b). The maximum increment of PRR is found over the drylands of NA and AU, followed by EA, SA and WMA. However, the PRR over the drylands of NF and SF is decreased over 20%, implying a growing contribution of external water vapour transport to the local precipitation.

On the whole, the global PCR indicates decreasing trends during the period from 1980–2015, while the PRR tends to increase.

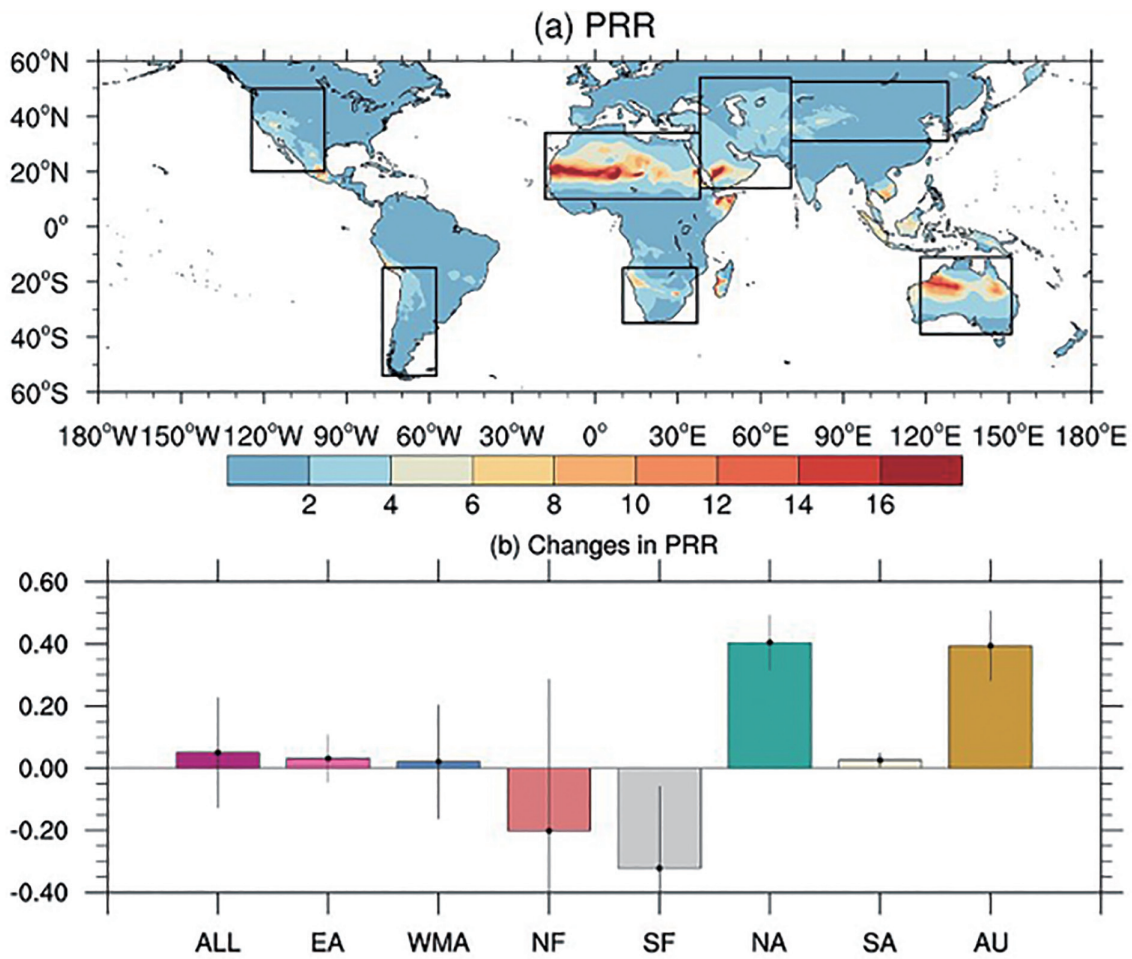


FIGURE 7 (a) Distribution of PRR (unit: %) and (b) the changes in the PRR over global drylands during period 1980–2015. The short straight lines in (b) denote the *SE*. The regions enclosed by rectangles in (a) denote the typical drylands in the globe, as described at the bottom of Figure 1 [Colour figure can be viewed at wileyonlinelibrary.com]

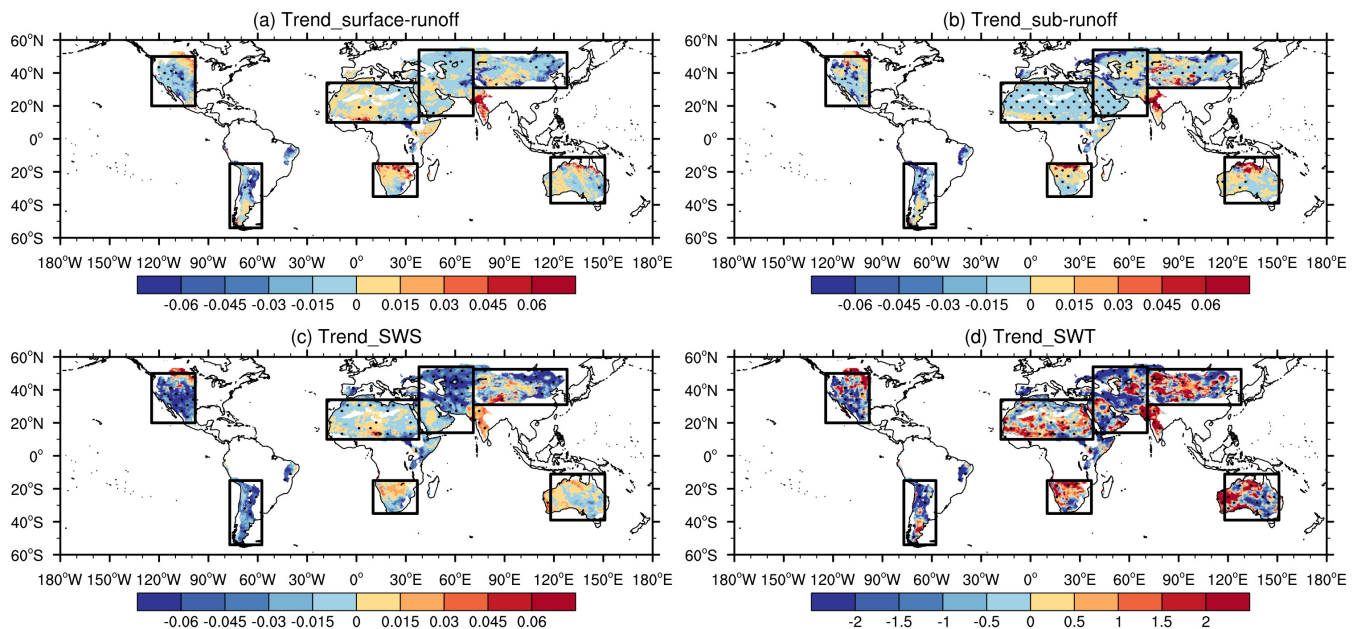


FIGURE 8 Trends (unit: mm-year⁻¹) of (a) surface runoff, (b) subsurface runoff, (c) surface soil water and (d) total soil water. The dots denote the trends are significant above the 90% confidence level. The regions enclosed by rectangles denote the typical drylands in the globe, as described at the bottom of Figure 1 [Colour figure can be viewed at wileyonlinelibrary.com]

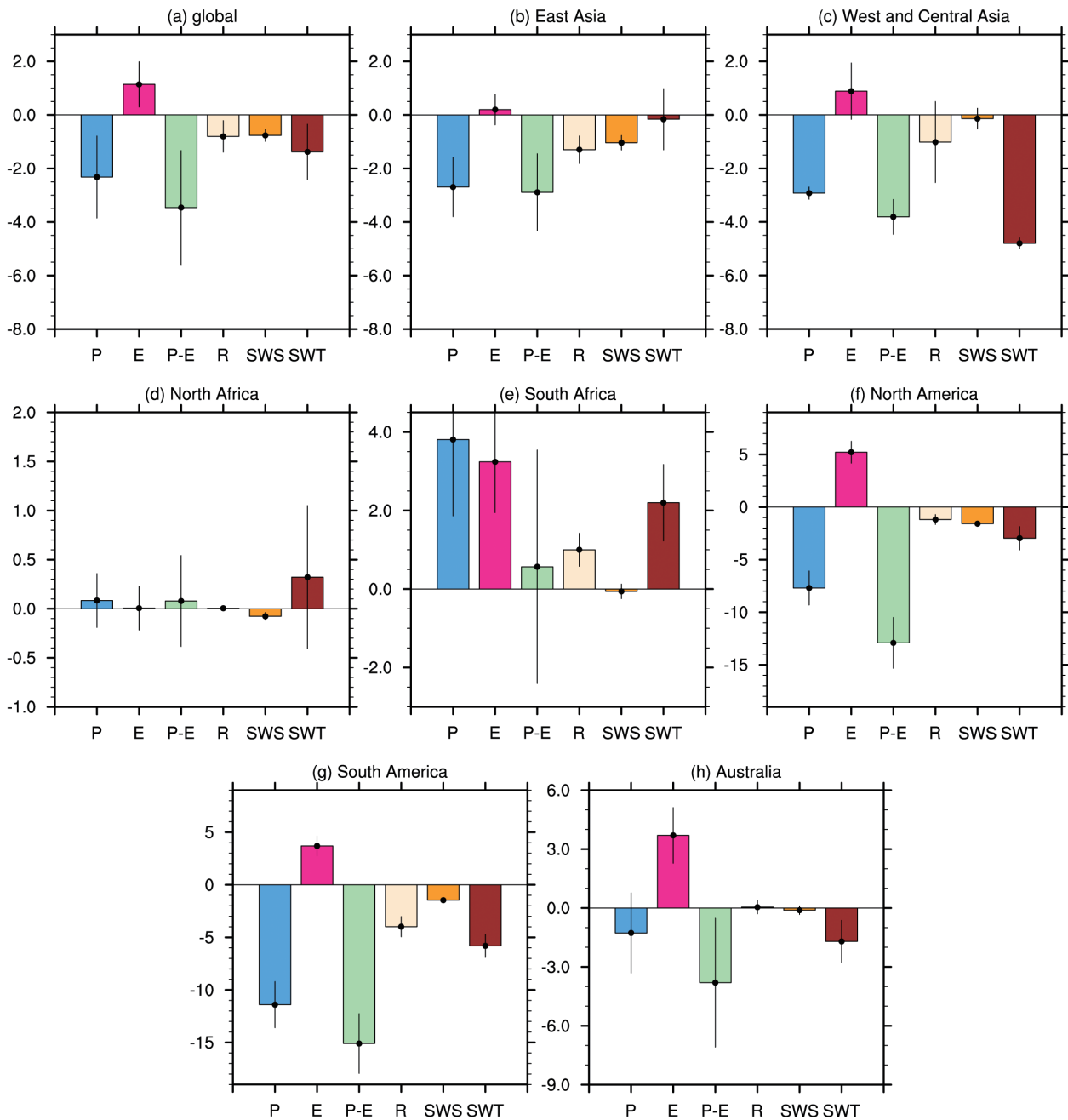


FIGURE 9 Changes (unit: mm) of precipitation (P), evaporation (E), the difference between precipitation and evaporation (P–E), total runoff (R), surface soil water (SWS) and total soil water (SWT) from 1980 to 2015. The total soil water is scaled by 1/10. The short straight lines in the bar denote the SE [Colour figure can be viewed at wileyonlinelibrary.com]

4.4 | Response of drylands' water-cycle

According to the theory of surface water balance, the runoff and SW are the other important components of water-cycle (Trenberth and Fasullo, 2013). The trends of runoff and SW are presented in Figure 8. The result shows that the trends of runoff (Figure 8a,b) and surface soil water (SWS) (Figure 8c) are in an agreement with the tendency of precipitation, the reason of which is that the water of runoff and SWS are primarily from

the precipitation. The trends of surface runoff and sub-surface runoff appear a maximum reduction with the value of $-0.06 \text{ mm}\cdot\text{year}^{-1}$ over the drylands of NA, SA, WMA and Northeast China. For the drylands of NF, SF, AU and Northwest China, the maximum increased value is about $0.06 \text{ mm}\cdot\text{year}^{-1}$ (Figure 8a,b). In addition, the trends of SWS are similar with that of runoff. The positive trends are mainly found over the drylands of AU, NF and SF with the mean value about $0.001 \text{ mm}\cdot\text{year}^{-1}$. Besides, the negative mean value

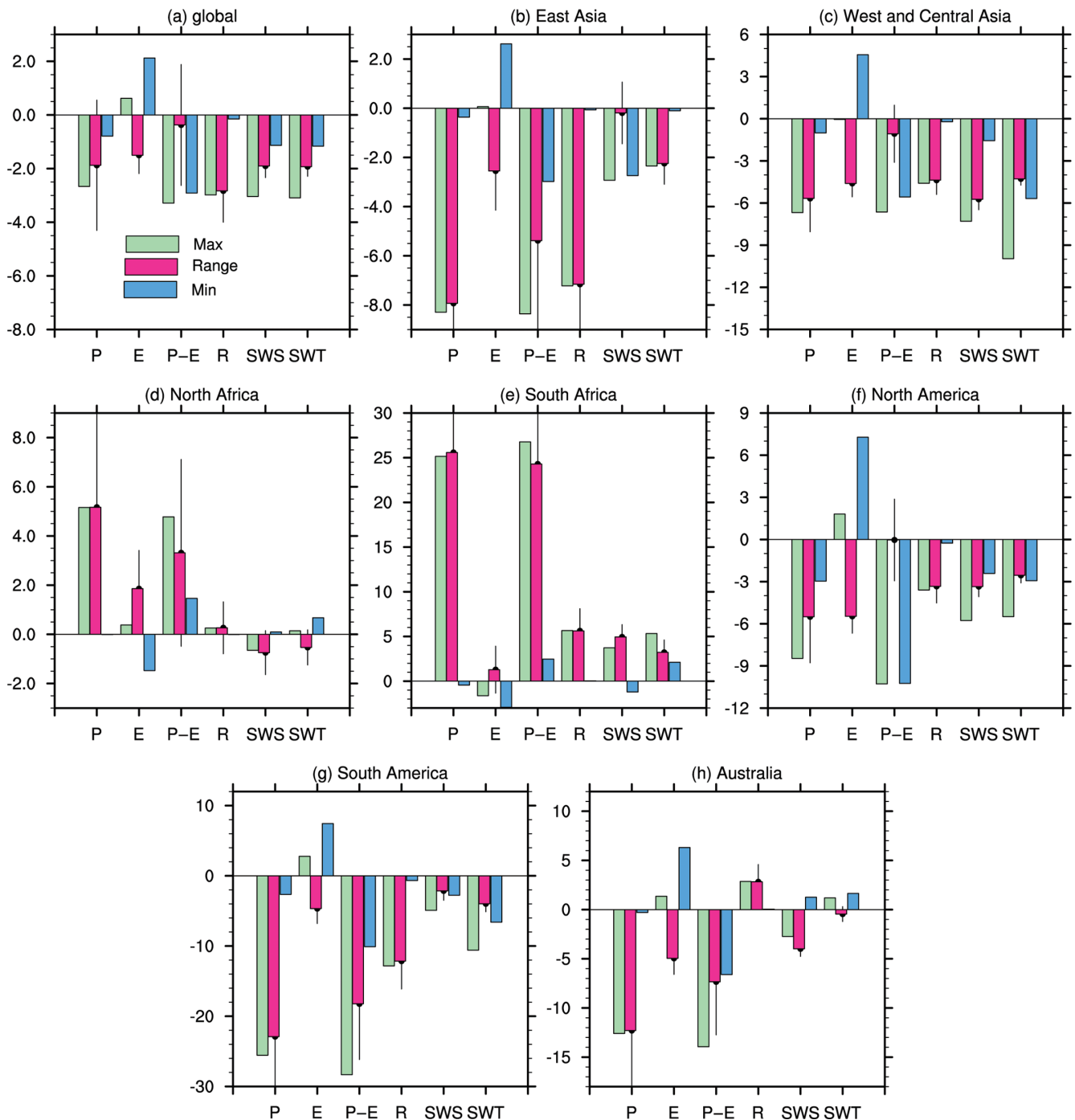


FIGURE 10 The annual range (unit: mm) (red bar), maximal (light green bar) and minimum (blue bar) changes of water cycle components over different drylands. The total soil water is scaled by 1/10. The short straight lines in the bar denote the SE [Colour figure can be viewed at wileyonlinelibrary.com]

about $-0.03 \text{ mm}\cdot\text{year}^{-1}$ is found over EA, WMA, NA and SA (Figure 8c). The total soil water (SWT) indicates a similar trend with SWS except for a greater magnitude of SWT than SWS and runoff. Such difference may be induced by the tight association of SWT with the soil texture, soil depth, and the underlying groundwater level.

Figure 9 gives the changes in precipitation, $P-E$, runoff, SWS and SWT from 1980 to 2015. The result shows that the precipitation over the global drylands decreases by -2.72 mm , while the evaporation increases by 1.84 mm during period 1980–2015. The decrease in precipitation and increase in evaporation cause the decrease in $P-E$ with -4.76 mm . The runoff and SWS present

negative changes, which are less than the change in precipitation (Figure 9a). On the contrary, the increased precipitation over the drylands of NF and SF can induce the increases in runoff and SWS (Figure 9d,e). Based on the surface water budget balance equation, the $P-E$ should offset the total runoff well, neglecting the changes in land surface water storage (Zhang *et al.*, 2019). However, the change in $P-E$ exceeds the total runoff over global drylands in this study. The imbalance mentioned above may mainly originate from the uncertainty of ERA5 data sets. Moreover, the changes in terrestrial water storage, which includes glaciers melting, lakes growing and land cover evolution, are still not clearly known due to the poor understanding on the soil texture, soil depth, and underlying groundwater level. These biases above commonly induce the imbalance of surface water budget.

In order to quantify the reduction of water-cycle over the global drylands, the AR is introduced further. As shown in Figure 10a, the values of AR for precipitation, evaporation, runoff, SWS and SWT indicate significantly decrease over the global drylands. For the drylands of NF and SF, the increased precipitation causes the intensified AR which implies an enhanced water-cycle (Figure 10d,e).

5 | CONCLUSIONS AND DISCUSSIONS

In this study, we investigate the characteristics and changes of water-cycle over the global drylands from 1980 to 2015. With the global warming, the mean SAT presents an increasing trend at a rate of $0.03 \text{ K}\cdot\text{year}^{-1}$. Consequently, the evaporation tends to increase, while the precipitation behaves differently. The mean value of increase in evaporation is about $1.1 \text{ mm}\cdot\text{year}^{-1}$ from 1980 to 2015, while the trends of decrease in precipitation and runoff are about -2.1 and $-0.8 \text{ mm}\cdot\text{year}^{-1}$ from 1980 to 2015 over the global drylands. The maximum increases in the precipitation and runoff are found over the drylands of SA and Northwest China, while the maximum decreases in them are found over the drylands of NA and SA.

The average PCR over the global drylands tends to decrease. The maximum reduction of PCR is found over the drylands of America and Asia, followed by the AU. Meanwhile, the PRR over the global drylands tends to increase by about 5% over the past 36 years from 1980 to 2015. The increased PRR is mainly found over the drylands of EA, WMA, NA, SA and AU, implying more local evaporation can convert into local precipitation. However, the PRR ranging from 4 to 16% shows decreasing trends over the drylands of NF and SF, indicating less

contribution of evaporation to the precipitation. The conclusion about the PRR is consistent with current findings (Li *et al.*, 2018; Yao *et al.*, 2020).

Basing on the comprehensive analysis, it is found that water-cycle is weakened over the most of global drylands from 1980 to 2015, while the water-cycle over the drylands of Africa is intensified. The anomalous water-cycle is closely related to the vertical velocity and circulations, in which the enhanced ascending motion over the drylands of NF and SF is in favour of intensifying the local water-cycle.

In this study, there still remains some uncertainties originated from the ERA5 reanalysis. Because of the lack of observational data of runoff and SW, there exists an imbalance in the surface water budget. In future study, collecting more observations and conducting model simulations are efficient means to reduce the bias for water-cycle analysis.

ACKNOWLEDGEMENTS

This research was mainly supported by the National Natural Science Foundation of China (41991231, 91744311, 41521004 and 91937302), Strategic Priority Research Program of the Chinese Academy of Sciences (XDA2006010301), and jointly supported by the Fundamental Research Funds for the Central Universities (lzujbky-2020-kb02). The authors declare no competing interests.

ORCID

Yuzhi Liu  <https://orcid.org/0000-0001-8310-6975>

Tianbin Shao  <https://orcid.org/0000-0001-9495-9180>

REFERENCES

- Abbott, B., Bishop, K., Zarnetske, J., Minaudo, C., Chapin, F., Krause, S., Hannah, D., Conner, L., Ellison, D., Godsey, S., Plont, S., Marcais, J., Kolbe, T., Huebner, A., Frei, R., Hampton, T., Gu, S., Buhman, M., Sayedi, S., Ursache, O., Chapin, M., Henderson, K. and Pinay, G. (2019) Human domination of the global water-cycle absent from depictions and perceptions. *Nature Geoscience*, 12(7), 533–540. <https://doi.org/10.1038/s41561-019-0374>.
- Albergel, C., Balsamo, G., de Rosnay, P., Muñoz-Sabater, J. and Boussetta, S. (2012) A bare ground evaporation revision in the ECMWF land-surface scheme: evaluation of its impact using ground soil moisture and satellite microwave data. *Hydrology and Earth System Sciences*, 16, 3607–3620. <https://doi.org/10.5194/hess-16-3607-2012>.
- Alfaro-Sánchez, R., Klesse, N.S., Hudson, A., Belmecheri, S., Köse, N., Diaz, H.F., Monson, R., Villalba, R. and Trouet, V. (2018) Climatic and volcanic forcing of tropical belt northern boundary over the past 800 years. *Nature Geoscience*, 11(12), 933–938. <https://doi.org/10.1038/s41561-018-0242-1>.
- Allan, R.P., Barlow, M., Byrne, M.P., Cherchi, A., Douville, H., Fowler, H.J., Gan, T.Y., Pendergrass, A.G., Rosenfeld, D.,

- Swann, A.L., Wilcox, L.J. and Zolina, O. (2020) Advances in understanding large-scale responses of the water-cycle to climate changes. *Annals of the New York Academy of Sciences*, 1472(1), 49–57. <https://doi.org/10.1111/nyas.14337>.
- Allan, R.P., Liu, C.L., Zahn, M., Levers, D.A., Koukouvagias, E. and Bodas-Salcedo, A. (2014) Physically consistent responses of the global atmospheric hydrological cycle in models and observations. *Surveys in Geophysics*, 35, 533–552. <https://doi.org/10.1007/s10712-012-9213-z>.
- Balsamo, G., Albergel, C., Beljaars, A., Boussetta, S., Brun, E., Cloke, H., Dee, D.P., Dutra, E., Muñoz Sabater, J., Pappenberger, F., de Rosnay, P., Stockdale, T. and Vitart, F. (2015) ERA-interim/land: a global land surface reanalysis data set. *Hydrology and Earth System Sciences*, 19(1), 389–407. <https://doi.org/10.5194/hess-19-389-2015>.
- Balsamo, G., Viterbo, P., Beljaars, A., van den Hurk, B., Hirschi, M., Betts, A. and Scipal, K. (2009) A revised hydrology for the ECMWF model: verification from field site to terrestrial water storage and impact in the integrated forecast system. *Journal of Hydrometeorology*, 10(3), 623–643. <https://doi.org/10.1175/2008JHM1068.1>.
- Bosilovich, M.G., Schubert, S.D. and Walker, G.K. (2005) Global changes of the water cycle intensity. *Journal of Climate*, 18(10), 1591–1608. <https://doi.org/10.1175/JCLI3357.1>.
- Boussetta, S., Balsamo, G., Beljaars, A., Kral, T. and Jarlan, L. (2013) Impact of a satellite-derived leaf area index monthly climatology in a global numerical weather prediction model. *International Journal of Remote Sensing*, 34(9–10), 3520–3542. <https://doi.org/10.1080/01431161.2012.716543>.
- Brohan, P., Kennedy, J.J., Harris, I., Tett, S.F. and Jones, P.D. (2006) Uncertainty estimates in regional and global observed temperature changes: a new data set from 1850. *Journal of Geophysical Research*, 111, D12106. <https://doi.org/10.1029/2005JD006548>.
- Brubaker, K.L., Entekhabi, D. and Eagleson, P.S. (1993) Estimation of continental precipitation recycling. *Journal of Climate*, 6(6), 1077–1089. [https://doi.org/10.1175/1520-0442\(1993\)006<1077:eocpr>2.0.co;2](https://doi.org/10.1175/1520-0442(1993)006<1077:eocpr>2.0.co;2).
- Burde, G.I. and Zangvil, A. (2001) The estimation of regional precipitation recycling. Part II: a new recycling model. *Journal of Climate*, 14(2), 2509–2527. [https://doi.org/10.1175/1520-0442\(2001\)014<2509:TEORPR>2.0.CO;2](https://doi.org/10.1175/1520-0442(2001)014<2509:TEORPR>2.0.CO;2).
- Chou, C. and Lan, C. (2012) Changes in the annual range of precipitation under global warming. *Journal of Climate*, 25, 222–235. <https://doi.org/10.1175/JCLI-D-11-00097.1>.
- Dwyer, J.G., Biasutti, M. and Sobel, A.H. (2014) The effect of greenhouse gas-induced changes in SST on the annual cycle of zonal mean tropical precipitation. *Journal of Climate*, 27(12), 4544–4565. <https://doi.org/10.1175/JCLI-D-13-00216.1>.
- Fontaine, B., Roucou, P. and Trzaska, S. (2003) Atmospheric water cycle and moisture fluxes in the west African monsoon: mean annual cycles and relationship using NCEP/NCAR reanalysis. *Geophysical Research Letters*, 30(3), 1117. <https://doi.org/10.1029/2002GL015834>.
- Fu, Q., Thorsen, T., Su, J., Ge, J. and Huang, J. (2009) Test of Mie-based single-scattering properties of non-spherical dust aerosols in radiative flux calculations. *Journal of Quantitative Spectroscopy and Radiative Transfer*, 110(14–16), 1640–1653. <https://doi.org/10.1016/j.jqsrt.2009.03.010>.
- Gimeno, L., Stohl, A., Trigo, R.M., Dominguez, F., Yoshimura, K., Yu, L., Drumond, A., Durán-Quesada, A.M. and Nieto, R. (2012) Oceanic and terrestrial sources of continental precipitation. *Reviews of Geophysics*, 50, 1–41. <https://doi.org/10.1029/2012RG000389>.
- Grafton, R., Williams, J., Perry, C., Molle, F., Ringler, C., Steduto, P., Udall, B., Wheeler, S., Wang, Y., Garrick, D. and Allen, R. (2018) The paradox of irrigation efficiency. *Science*, 361(6404), 748–750. <https://doi.org/10.1126/science.aat9314>.
- Guan, X., Huang, J., Guo, R. and Lin, P. (2015) The role of dynamically induced variability in the recent warming trend slowdown over the northern hemisphere. *Scientific Reports*, 5, 12669. <https://doi.org/10.1038/srep12669>.
- Guo, Y.P. and Wang, C.H. (2014) Trends in precipitation recycling over the Qinghai – Xizang plateau in last decades. *Journal of Hydrology*, 517(19), 826–835. <https://doi.org/10.1016/j.jhydrol.2014.06.006>.
- Han, X., Xue, H., Zhao, C. and Lu, D. (2016) The roles of convective and stratiform precipitation in the observed precipitation trends in Northwest China during 1961–2000. *Atmospheric Research*, 169, 139–146. <https://doi.org/10.1016/j.atmosres.2015.10.001>.
- Hersbach, H., Bell, B., Berrisford, P., Hirahara, S., Horányi, A., Muñoz-Sabater, J., Nicolas, J., Peubey, C., Radu, R., Schepers, D., Simmons, A., Soci, C., Abdalla, S., Abellan, X., Balsamo, G., Bechtold, P., Biavati, G., Bidlot, J., Bonavita, M., Chiara, G., Dahlgren, P., Dee, D., Diamantakis, M., Dragani, R., Flemming, J., Forbes, R., Fuentes, M., Geer, A., Haimberger, L., Healy, S., Hogan, R.J., Hólm, E., Janisková, M., Keeley, S., Laloyaux, P., Lopez, P., Lupu, C., Radnoti, G., Rosnay, P., Rozum, I., Vamborg, F., Villaume, S. and Thépaut, J. (2020) The ERA5 global reanalysis. *Quarterly Journal of the Royal Meteorological Society*, 146(730), 1999–2049. <https://doi.org/10.1002/qj.3803>.
- Hua, S., Liu, Y., Jia, R., Chang, S., Wu, C., Zhu, Q., Shao, T. and Wang, B. (2018) Role of clouds in accelerating cold-season warming during 2000–2015 over the Tibetan plateau. *International Journal of Climatology*, 38, 4950–4966. <https://doi.org/10.1002/joc.5709>.
- Huang, J., Ji, M., Xie, Y., Wang, S., He, Y. and Ran, J. (2016b) Global semi-arid climate change over last 60 years. *Climate Dynamics*, 46(3–4), 1131–1150. <https://doi.org/10.1007/s00382-015-2636-8>.
- Huang, J., Li, Y., Fu, C., Chen, F., Fu, Q., Dai, A., Shinoda, M., Ma, Z., Guo, W., Li, Z., Zhang, L., Liu, Y., Yu, H., He, Y., Xie, Y., Guan, X., Ji, M., Lin, L., Wang, S., Yan, H. and Wang, G. (2017) Dryland climate change: recent progress and challenges. *Reviews of Geophysics*, 55, 719–778. <https://doi.org/10.1002/2016RG000550>.
- Huang, J., Liu, X., Li, C., Ding, L. and Yu, H. (2018) The global oxygen budget and its future projection. *Science Bulletin*, 63, 1180–1186. <https://doi.org/10.1016/j.scib.2018.07.023>.
- Huang, J., Yu, H., Guan, X., Wang, G. and Guo, R. (2016a) Accelerated dryland expansion under climate change. *Nature Climate Change*, 6, 166–171. <https://doi.org/10.1038/nclimate2837>.
- Huang, J., Zhang, W., Zuo, J., Bi, J., Shi, J., Wang, X., Chang, Z., Huang, Z., Yang, S., Zhang, B., Wang, G., Feng, G., Yuan, J., Zhang, L., Zuo, H., Wang, S., Fu, C. and Chou, J. (2008) An overview of the semi-arid climate and environment research observatory over the loess plateau. *Advances in Atmospheric*

- Sciences*, 25(6), 1–16. <https://doi.org/10.1007/s00376-008-0906-7>.
- Hulme, M. (1996) Recent climatic change in the world's drylands. *Geophysical Research Letters*, 23(1), 61–64. <https://doi.org/10.1029/95gl03586>.
- IPCC. (2013) *Climate Change 2013: The Physical Science Basis. Contribution of Working Group I to the Fifth Assessment Report of the Intergovernmental Panel on Climate Change*. Cambridge: Cambridge University Press.
- Lei, H., Matai, H. and Jian, Z. (2015) The relationship between near 50a low cloud cover variation and meteorological factors in Xinjiang Aletai area. *Climate Change Research Letters*, 4, 32–41. <https://doi.org/10.12677/CCRL.2015.41004>.
- Li, J., Xie, S., Cook, E.R., Chen, F., Shi, J., Zhang, D.D., Fang, K., Gou, X., Li, T., Peng, J., Shi, S. and Zhao, Y. (2019) Deciphering human contributions to Yellow River flow reductions and downstream drying using centuries-long tree ring records. *Geophysical Research Letters*, 46(2), 898–905. <https://doi.org/10.1029/2018GL081090>.
- Li, R., Wang, C. and Wu, D. (2018) Changes in precipitation recycling over arid regions in the northern hemisphere. *Theoretical and Applied Climatology*, 131(1–2), 489–502. <https://doi.org/10.1007/s00704-016-1978-4>.
- Liu, Y., Hua, S., Jia, R. and Huang, J. (2019a) Effect of aerosols on the ice cloud properties over the Tibetan plateau. *Journal of Geophysical Research – Atmospheres*, 124, 9594–9608. <https://doi.org/10.1029/2019JD030463>.
- Liu, Y., Li, Y., Huang, J., Wang, S. and Zhu, Q. (2019c) Attribution of Tibetan plateau to the northern drought. *National Science Review*, 7(3), 489–492.
- Liu, Y., Luo, R., Zhu, Q.Z., Hua, S. and Wang, B. (2019d) Cloud ability to produce precipitation over arid and semiarid regions of central and East Asia. *International Journal of Climatology*, 40, 1–14. <https://doi.org/10.1002/joc.6304>.
- Liu, Y., Wu, C., Jia, R. and Huang, J. (2018) An overview of the influence of atmospheric circulation on the climate in arid and semi-arid region of central and East Asia. *Science China Earth Sciences*, 61, 1183–1194. <https://doi.org/10.1007/s11430-017-9202-1>.
- Liu, Y., Zhu, Q., Huang, J., Hua, S. and Jia, R. (2019b) Impact of dust-polluted convective clouds over the Tibetan plateau on downstream precipitation. *Atmospheric Environment*, 209, 67–77. <https://doi.org/10.1016/j.atmosenv.2019.04.001>.
- Luo, M., Liu, Y., Zhu, Q., Tang, Y. and Alam, K. (2020a) Role and mechanisms of black carbon affecting water vapor transport to Tibet. *Remote Sensing*, 12, 231. <https://doi.org/10.3390/rs12020231>.
- Luo, M., Ning, G., Xu, F., Wang, S., Liu, Z. and Yang, Y. (2020b) Observed heatwave changes in arid Northwest China: physical mechanism and long-term trend. *Atmospheric Research*, 242, 105009. <https://doi.org/10.1016/j.atmosres.2020.105009>.
- Pelosi, A., Terribile, F., D'Urso, G. and Chirico, G.B. (2020) Comparison of ERA5-land and UERRA MESCAN-SURFEX reanalysis data with spatially interpolated weather observations for the regional assessment of reference evapotranspiration. *Water*, 12(6), 1669. <https://doi.org/10.3390/w12061669>.
- Ping, L., Guoxiong, W. and Shufen, S. (2001) Local meridional circulation and deserts. *Advances in Atmospheric Sciences*, 18, 864–872. <https://doi.org/10.1007/BF03403508>.
- Qi, Y., Ge, J. and Huang, J. (2013) Spatial and temporal distribution of MODIS and MISR aerosol optical depth over northern China and comparison with AERONET. *Chinese Science Bulletin*, 58(20), 2497–2506. <https://doi.org/10.1007/s11434-013-5678-5>.
- Scheffer, M., Carpenter, S., Foley, J.A., Folke, C. and Walker, B. (2001) Catastrophic shifts in ecosystems. *Nature*, 413(6856), 591–596. <https://doi.org/10.1038/35098000>.
- Shin, S.H., Chung, I.U. and Kim, H.J. (2012) Relationship between the expansion of drylands and the intensification of Hadley circulation during the late twentieth century. *Meteorology and Atmospheric Physics*, 118(3–4), 117–128. <https://doi.org/10.1007/s00703-012-0220-x>.
- Skirris, N., Marsh, R., Mecking, J. and Zika, J. (2020) Changing water cycle and freshwater transports in the Atlantic Ocean in observations and CMIP5 models. *Climate Dynamics*, 54(11–12), 4971–4989. <https://doi.org/10.1007/s00382-020-05261-y>.
- Song, F., Zhou, T. and Qian, Y. (2014) Responses of east Asian summer monsoon to natural and anthropogenic forcings in the 17 latest CMIP5 models. *Geophysical Research Letters*, 41(2), 596, GL058705–603. <https://doi.org/10.1002/2013>.
- Su, T., Lu, Z., Zhou, J., Hou, W., Li, Y. and Tu, G. (2014) Spatial distribution and seasonal variation characteristics of global atmospheric moisture recycling. *Acta Physica Sinica*, 63(9), 099201. <https://doi.org/10.7498/aps.63.099201>.
- Trenberth, K.E. and Fasullo, J.T. (2013) Regional energy and water-cycles: transports from ocean to land. *Journal of Climate*, 26, 7837–7851. <https://doi.org/10.1175/JCLI-D-13-00008.1>.
- Wang, B., Liu, J., Kim, H., Webster, P.J. and Yim, S. (2012) Recent change of the global monsoon precipitation (1979–2008). *Climate Dynamics*, 39(5), 1123–1135. <https://doi.org/10.1007/s00382-011-1266-z>.
- Wang, W., Huang, J., Zhou, T., Bi, J., Lin, L., Chen, Y., Huang, Z. and Su, J. (2013) Estimation of radiative effect of a heavy dust storm over Northwest China using Fu-Liou model and ground measurements. *Journal of Quantitative Spectroscopy and Radiative Transfer*, 122, 114–126. <https://doi.org/10.1016/j.jqsrt.2012.10.018>.
- Xiang, H., Zhang, F., Jiang, J., Peng, J., Zhang, X. and Zhang, C. (2014) Analysis of global cloud amount over the past 30 years based on CFSR data. *Meteorological Monthly (in Chinese)*, 40(5), 555–561. <https://doi.org/10.7519/j.issn.1000-0526.2014.05.005>.
- Xu, D., Kong, Y. and Wang, C.H. (2016) Water vapor budget in arid area of Northwest China and It's relationship with precipitation. *Journal of Arid Meteorology*, 34(3), 431–439. [https://doi.org/10.11755/j.issn.1006-7639\(2016\)-03-0431](https://doi.org/10.11755/j.issn.1006-7639(2016)-03-0431).
- Yao, J., Chen, Y., Zhao, Y., Guan, X., Mao, W. and Yang, L. (2020) Climatic and associated atmospheric water cycle changes over the Xinjiang, China. *Journal of Hydrology*, 585, 124823. <https://doi.org/10.1016/j.jhydrol.2020.124823>.
- Yin, D. and Roderick, M. (2020) Inter-annual variability of the global terrestrial water cycle. *Hydrology and Earth System Sciences*, 24(1), 381–396. <https://doi.org/10.5194/hess-24-381-2020>.
- Zhang, W., Zhou, T., Zhang, L. and Zou, L. (2019) Future intensification of the water cycle with an enhanced annual cycle over global land monsoon regions. *Journal of Climate*, 32(17), 5437–5452. <https://doi.org/10.1175/JCLI-D-18-0628.1>.
- Zhang, X., Li, M.X. and Ma, Z.G. (2018) Evapotranspiration variability over global arid and semi-arid regions from 1982 to

2011. *Chinese Journal of Atmospheric Sciences*, 42(2), 251–267.
<https://doi.org/10.3878/j.issn.1006-9895.1709.16288>.

Zhou, C., Zhao, P. and Chen, J. (2019) The Interdecadal Change of summer water vapor over the Tibetan plateau and associated mechanisms. *Journal of Climate*, 32, 4103–4119. <https://doi.org/10.1175/JCLI-D-18-0364.1>.

How to cite this article: Luo M, Liu Y, Shao T. Response of drylands' water-cycle to the global warming. *Int J Climatol*. 2021;41:4587–4602.
<https://doi.org/10.1002/joc.7088>